

Microwave Admittance of Gold-Palladium Nanowires with Proximity-Induced Superconductivity

Russell E. Lake,¹ Joonas Govenius,¹ Roope Kokkonen,¹ Kuan Yen Tan,¹ Matti Partanen,¹ Pauli Virtanen,^{2,3} and Mikko Möttönen¹

¹*QCD Labs, COMP Centre of Excellence, Department of Applied Physics, Aalto University, P.O. Box 13500, FI-00076 Aalto, Finland*

²*Low Temperature Laboratory, Department of Applied Physics, P.O. Box 15100, FI-00076 Aalto University, Finland*

³*NEST, Istituto Nanoscienze-CNR and Scuola Normale Superiore, I-56127 Pisa, Italy*

We report quantitative electrical admittance measurements of diffusive superconductor–normal-metal–superconductor (SNS) junctions at gigahertz frequencies and millikelvin temperatures. The gold-palladium-based SNS junctions are arranged into a chain of superconducting quantum interference devices. The chain is coupled strongly to a multimode microwave resonator with a mode spacing of approximately 0.6 GHz. By measuring the resonance frequencies and quality factors of the resonator modes, we extract the dissipative and reactive parts of the admittance of the chain. We compare the phase and temperature dependence of the admittance near 1 GHz to theory based on the time-dependent Usadel equations. This comparison allows us to identify important discrepancies between theory and experiment that are not resolved by including inelastic scattering or elastic spin-flip scattering in the theory.

I. INTRODUCTION

The transport of direct current (dc) between two superconductors (S) separated by a diffusive normal-metal (N) link is in general well understood both theoretically and experimentally.^{1–6} At low temperatures and currents, Andreev reflection⁷ leads to the formation of a gap in the density of quasiparticle states in N and allows a dissipationless supercurrent to flow. This gap has been directly observed in tunnel spectroscopy measurements.^{8,9} Shapiro steps, supercurrent enhancement, and other non-equilibrium effects under intense microwave irradiation have also been extensively studied.^{1,10–16}

In contrast, the near-equilibrium response of superconductor–normal-metal–superconductor (SNS) junctions to weak microwave radiation has become an active area of investigation only recently.^{17–21} While the adiabatic contribution to the kinetic inductance can be calculated from the dc current–phase relation, at high frequencies both reactive and dissipative contributions also arise from other mechanisms, such as driven transitions between quasiparticle states and oscillation of the Andreev level populations.¹⁸ Surprisingly however, little experimental data has been published on the topic thus far.^{22,23} The parameter regimes and materials studied in the published experiments are very sparse, hence limiting the extent to which theoretical predictions^{17–21} can be tested. In practice, data on the effective inductance and losses also expedites the process of designing high-frequency SNS-junction-based circuits, such as the SNS nanobolometer.^{24,25}

Previous experimental studies^{22,23} have probed flux- and temperature-dependent changes in the linear microwave response of a superconducting ring with a gold normal-metal inclusion. The superconducting ring consisted of ion-beam-deposited tungsten in the first experiments,²² and sputter-deposited Nb with a thin Pd

layer at the SN interface in the later experiments.²³ A single SNS ring was biased with a dc magnetic flux and coupled weakly to a multi-mode microwave resonator. By measuring flux-dependent shifts in the quality factors and resonance frequencies, the authors determined how the complex-valued electrical susceptibility χ changes.^{22,23} The change in χ , as a function of flux and temperature, was reported to be in excellent agreement with theoretical predictions based on Usadel equations and numerical simulations. However, the implicit offsets in both the real and imaginary parts of the reported susceptibility prevent a comparison to the theoretically predicted absolute values of $\text{Re}[\chi]$ and $\text{Im}[\chi]$. They also prevent the accurate prediction of the effective inductance ($\text{Re}[\chi]^{-1}$) and the loss tangent ($\text{Im}[\chi]/\text{Re}[\chi]$), which are the key quantities for any practical high-frequency application of SNS junctions.

In this article, we present measurements of the SNS junction admittance $Z^{-1}(\omega) = \chi/i\omega$ for gold-palladium based junctions at angular frequencies ω of order $2\pi \times 1$ GHz. We use a chain of SNS superconducting quantum interference devices (SQUIDs) with a strong capacitive coupling to a multimode microwave resonator with a typical mode spacing of 0.6 GHz. Each chain consists of 20 SNS SQUIDs in series. The strong coupling and the large number of SQUIDs lead to significant changes in the frequencies and quality factors of the resonator modes, which allow determining Z^{-1} without an offset. The absence of an offset enables us to show that the Usadel-equation-based theory we consider cannot simultaneously explain the observed real and imaginary parts of Z^{-1} .

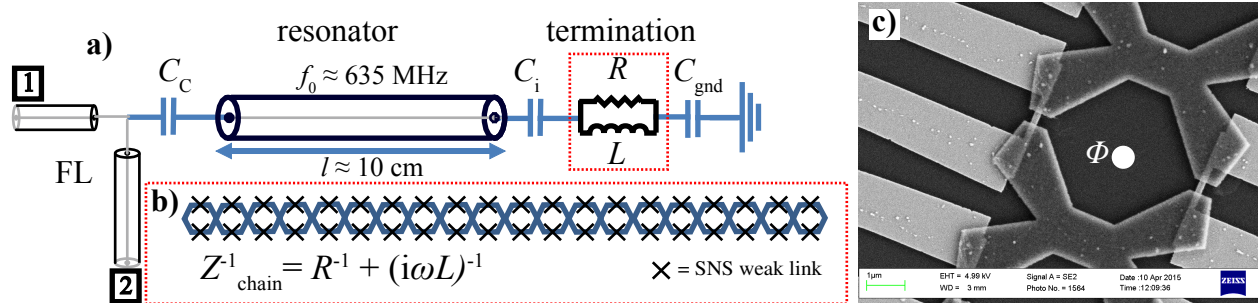


FIG. 1. a) On-chip circuit layout: feedline (FL) between ports 1 and 2, transmission line part of the resonator, and termination. The resonances are externally damped by the capacitive coupling (C_C) to the feedline, and internally damped by the capacitively coupled SQUID chain. See Table I for further details on parameter values. b) Schematic detail of the device under test at the termination: 20 SNS SQUIDs in series. c) Micrograph of a single SQUID from a sample fabricated identically to Sample 2. The wide Au-Pd extensions (light colored regions) are heat sinks.

II. SAMPLES

We study the linear electrical response of SNS junctions at millikelvin temperatures in two samples: Sample 1 and 2. The gold-palladium nanowires used as the normal-metal are deposited simultaneously in the same fabrication steps as for our recent nanobolometer circuits.²⁵ We determine the Au:Pd atomic ratio of the alloy to be approximately 3:2 using energy-dispersive X-ray spectroscopy (see Section VII A 3). The nominal junction length l is 300 nm and the nominal cross-sectional area is 30 nm \times 120 nm. The normal-state resistance of a single junction $R_N = 15 \Omega$ is estimated based on four-wire dc measurements of reference samples. From the reference measurements, we also estimate the upper bound for the contact resistance R_B to be approximately $\lesssim 1 \Omega$. We only give an upper bound for the contact resistance because of the uncertainties introduced by the crossed-wire geometry²⁶ of the reference samples. Reference samples are similar to those in Figure 1b in Reference 25.

The key parameter determining the strength of the proximity-induced superconductivity is the Thouless energy $E_T = \hbar D l^{-2}$, where $D \approx 22 \text{ cm}^2 \text{ s}^{-1}$ is the diffusion constant. In our samples, the Thouless energy is $E_T \approx k_B \times 190 \text{ mK} \approx \hbar \times 3.9 \text{ GHz}$, where $\hbar = 2\pi\hbar$ and k_B is the Boltzmann constant. The superconducting sections are 100-nm thick aluminum, which implies that the energy gap Δ in the superconductors is much larger than the Thouless energy ($\Delta/E_T \approx 13$). Both S and N parts are fabricated using electron beam lithography and evaporation. Further fabrication details are reported in the Experimental Section VII A.

The SNS junctions are arranged into a chain of SQUIDs, as shown in Figure 1. Each SQUID loop has a relatively small area of 20 μm^2 in order to minimize sensitivity to external magnetic field noise. In addition, we measured Sample 2 in a double layer magnetic shield. The geometric inductance of each loop is small ($L_G < 10 \text{ pH}$) compared to the effective inductance of the SQUID, as verified by the results below. A dc magnetic flux bias

is applied by an external coil that provides a uniform flux bias Φ for each SQUID in the 100 μm long chain. Assuming identical junctions, this phase biases each SNS junction to $\pi(\Phi - m\Phi_0)/\Phi_0$ at dc, where Φ_0 is the magnetic flux quantum $h/2e$ and m is the integer that minimizes $|\Phi - m\Phi_0|$. We note that the flux bias we label as $\Phi = 0$ may be offset from the true zero flux condition by an integer multiple of Φ_0 .

The SQUID chains in the two samples are nominally identical, except for the addition of heat sinks to Sample 2 (see Figure 1c). The heat sinks are designed to reduce the hot-electron effect,²⁷ i.e., the increase of the quasiparticle temperature above the phonon bath temperature T_b that we measure. For each SNS junction, the heat sink consist of two large (0.5 μm^3) reservoirs of gold-palladium that are thermally strongly coupled to the junction.

In addition to the SQUID chain, the chip contains a transmission line resonator (see Figure 1a and Table I). We characterize it by measuring control samples with an open termination, i.e., samples without the SQUID chain. From the control measurements, we extract the fundamental frequency of the transmission line resonator $f_0 \approx 635 \text{ MHz}$, and confirm that the internal quality factor $Q_{i,n} > 10^4$ for the resonances we consider ($n \sim 3$). The latter implies that we can neglect the losses in the transmission line part of the resonator, and in the Al_2O_3 used as the dielectric material in the lumped element capacitors (C_C and C_i). This is valid because introducing the SQUID chain lowers $Q_{i,n}$ to the order of 10^2 , as observed below. We also deduce the characteristic impedance $Z_0 \approx 39 \Omega$ of the transmission line from the measured f_0 , the length of the resonator, and the design value for the inductance per unit length.

TABLE I. Resonator and coupling capacitor parameters for Samples 1 and 2: the transmission line resonator length l_r and the internal (external) load capacitance C_i (C_C) shown in Figure 1. The last column emphasizes that Sample 2 includes additional large gold-palladium heat sink reservoirs for enhancing electron-phonon coupling.

Sample	C_C (pF)	C_i (pF)	l_r (mm)	f_0 (MHz)	Z_0 (Ω)	Heat sinks
1	0.15	14.5	97.2	637	39	No
2	0.44	15.2	96.5	633	39	Yes

III. MEASUREMENT SCHEME AND SAMPLE CHARACTERIZATION

We determine the admittance of the SQUID chain by embedding it as the termination of a long (10 cm) transmission line microwave resonator, as illustrated in Figure 1a. We first determine the resonance frequency f_n and the internal quality factor $Q_{i,n}$ of each mode n by measuring the frequency-dependent transmission coefficient $S_{21}(f)$ through the feedline. By comparing f_n and $Q_{i,n}$ to values measured in control samples, we can determine the admittance of the SQUID chain at multiple frequencies. Specifically, we use a circuit model (Figure 1a) that allows extracting the admittance of the SQUID chain Z_{chain}^{-1} from the response of the combined resonator/SQUID-chain system. The admittance of each individual SNS junction is then given by $10Z_{\text{chain}}^{-1}$, assuming that the junctions are identical and that geometric inductance is negligible.

Figure 2 shows the normalized transmission through the feedline at frequencies near 1.4 GHz, probing the third ($n = 3$) mode in Sample 2. The normalization (defined precisely in Section VII C) removes all spurious features in the transmission data that do not depend on flux. What remains is the oscillatory flux dependence of the resonance frequency f_n with a period we identify as Φ_0 . As the flux bias is increased away from integer multiples of Φ_0 , we measure a decrease in both the resonance frequency and the loaded quality factor $Q_{0,n}$. This behavior is more clearly visible in Figure 2b,c with individual slices of transmission data for $\Phi/\Phi_0 = 0$ and $\Phi/\Phi_0 = 0.3$. These changes in the resonance indicate that both the inductance and the losses increase in the SQUID chain near half-integer values of Φ/Φ_0 .

To extract f_n and $Q_{i,n}$ quantitatively, we fit the measured normalized transmission for the n^{th} mode to the model

$$S_{21}(f) = 1 - \frac{Q_{0,n} - 2iQ_{0,n}\frac{\delta f}{f_n}}{1 + 2iQ_{0,n}\frac{f-f_n}{f_n}}, \quad (1)$$

where δf is a fit parameter that characterizes asymmetry, and the external quality factor $Q_{C,n}$ is governed by the coupling (C_C) to the feedline.^{28,29} From the obtained fit parameters $Q_{0,n}$ and $Q_{C,n}$, we compute the contribution of losses due to the SQUID chain as $Q_{i,n}^{-1} = Q_{0,n}^{-1} - Q_{C,n}^{-1}$. Figure 3 shows the extracted values of f_n and $Q_{i,n}$ for frequencies up to 12 GHz ($n \approx 20$).

In the low-frequency and low-temperature regime, the SQUID chain behaves like an inductor, i.e., most of the

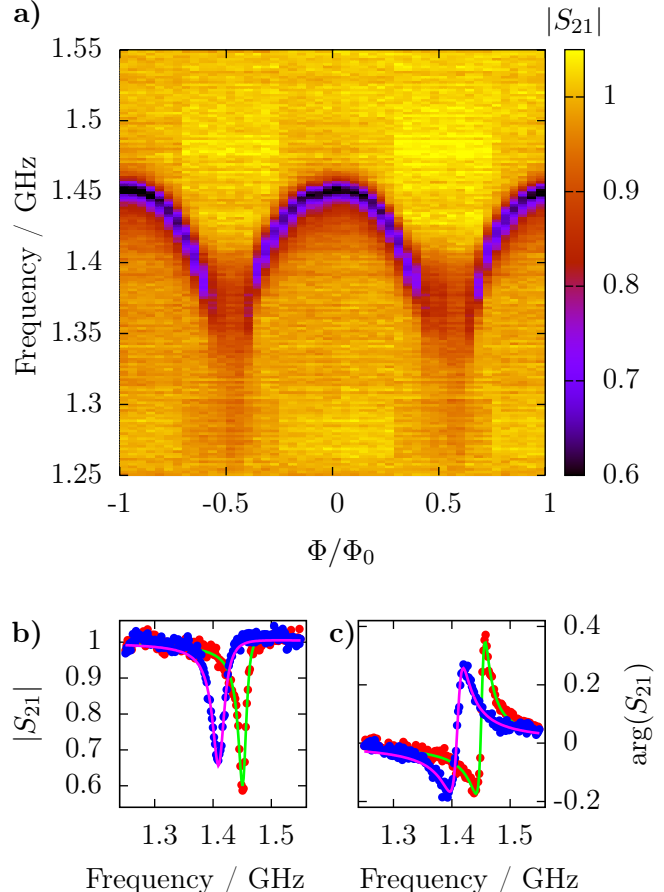


FIG. 2. a) Magnitude of the normalized transmission coefficient $|S_{21}|$ for the third resonator mode ($n = 3$) of Sample 2 at $T_b = 10$ mK as a function of frequency and flux-bias Φ . b) Traces from a) along $\Phi/\Phi_0 = 0$ and $\Phi/\Phi_0 = 0.3$ with fits (solid lines) to the model in Equation 1. c) Same as b) but for the phase $\arg(S_{21})$. The extracted resonance frequencies and internal quality factors are $f_3 = (1452.6 \pm 0.4)$ MHz; $Q_{i,3} = 127 \pm 8$ and $f_3 = (1411.1 \pm 0.4)$ MHz; $Q_{i,3} = 78 \pm 4$ for $\Phi/\Phi_0 = 0$ and $\Phi/\Phi_0 = 0.3$, respectively. The discontinuities in the background in a) are artifacts caused by the normalization procedure of S_{21} (see Section VII C).

admittance is reactive ($\text{Im}[Z_{\text{chain}}^{-1}] \gg \text{Re}[Z_{\text{chain}}^{-1}]$) and $\text{Im}[\omega Z_{\text{chain}}^{-1}]$ varies slowly as a function of the angular frequency $\omega = 2\pi f$. Consequently, we parametrize the admittance Z_{chain}^{-1} as a parallel combination of a resistor and an inductor, such that $Z_{\text{chain}}^{-1} = R^{-1} + (i\omega L)^{-1}$. Figure 3 demonstrates that this is a good parametrization by showing qualitative agreement between the experimental

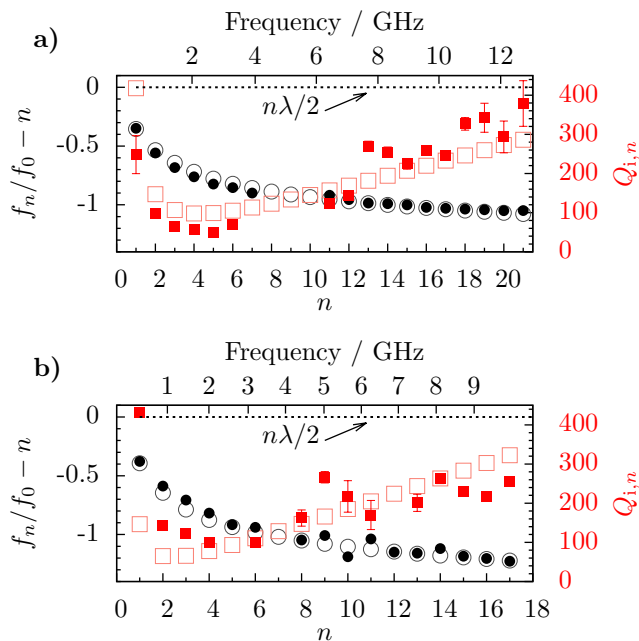


FIG. 3. Measured mode shift $f_n/f_0 - n$ (filled black circles) and internal quality factor $Q_{i,n}$ (filled red squares) for a) Sample 1 and b) Sample 2 at 10-mK phonon bath temperature and zero flux bias. For reference, the open markers show the theoretical prediction based on Equation 2 for a simplistic SQUID chain admittance $Z_{\text{chain}}^{-1} = R^{-1} + (i\omega L)^{-1}$ with a constant R equal to 350 Ω (500 Ω) and a constant L equal to 2.5 nH (5.0 nH) for Sample 1 (2). The dashed lines emphasize that the mode shift is zero for all harmonics of an ideal $\lambda/2$ resonator. Some f_n and $Q_{i,n}$ values could not be experimentally extracted due to the presence of nearby parasitic resonances.

data and predictions for the mode shifts and quality factors using a simplified model where L and R are constant.

Let us now discuss the extraction of the admittance Z_{chain}^{-1} from the measured f_n and $Q_{i,n}$ values. For an ideal transmission line resonator with open-circuit conditions at both ends ($C_C = C_i = 0$), the n^{th} mode is located at frequency nf_0 . In contrast, for the samples with the SQUID chains, the frequency-dependent reactive, i.e., imaginary parts of the termination admittances $i\omega C_C$ and $[(i\omega C_i)^{-1} + Z_{\text{chain}}]^{-1}$ lead to the non-zero modeshift of Figure 3, that we use to determine $\text{Im}[Z_{\text{chain}}^{-1}]$. Similarly, the measured $Q_{i,n}$ gives information about the dissipative, i.e., real part of Z_{chain}^{-1} .

Quantitatively, we determine the SQUID chain admittance Z_{chain}^{-1} from $\omega_n = 2\pi f_n$ and $Q_{i,n}$ by numerically solving the transcendental equation

$$i \tan \left[\frac{\omega_n}{2f_0} \left(1 + \frac{i}{2Q_{i,n}} \right) + \arctan(Z_0 \omega_n C_C) \right] = - \frac{Z_0}{(i\omega_n C_i)^{-1} + Z_{\text{chain}}(\omega_n)}, \quad (2)$$

using the parameters given in Table I. We derive this equation from the circuit model shown in Figure 1, as-

TABLE II. SQUID chain admittance $R^{-1} + (i\omega L)^{-1}$ and corresponding loss tangent $\omega L/R$ measured at $T_b = 10$ mK and $\Phi = 0$ for the second (third) resonance in Sample 1 (2). The effective inductance (resistance) per single SNS junction is $L/10$ ($R/10$).

Sample	f_n (GHz)	R (Ω)	L (nH)	$2\pi f_n L/R$
1	0.914	310 ± 30	3.4 ± 0.3	0.062
2	1.452	590 ± 50	3.1 ± 0.7	0.048

suming that $Q_{i,n}$ is dominated by losses in the SQUID chain.

Table II shows the L and R extracted for two examples resonances near 1 GHz. The reported values provide an important reference for designing high-frequency devices based on gold-palladium SNS junctions. That is, they imply that an effective inductance of a few hundred picohenries per junction and a loss tangent of a few percent can be expected around 1 GHz at millikelvin temperatures.

IV. THEORY

In the next section, we compare the experimental results to theoretical predictions¹⁸ based on the time-dependent Usadel equation.² In the low-frequency and low-temperature regime $\hbar\omega, k_B T \lesssim E_T$ considered below, the imaginary part of the admittance of the junction is expected to be mostly determined by the adiabatic Josephson inductance associated with the supercurrent, i.e., the Φ derivative of the dc supercurrent. The real part, on the other hand, mainly arises from driven quasiparticle transitions in the junction. The availability of such transitions is sensitive to the density of quasiparticle states. In particular, the presence of a proximity-induced energy gap $E_g \sim E_T$ in the density of states should lead to an exponential increase in the resistance as $k_B T$ decreases below E_g .

However, the low-temperature values of L and R^{-1} we measure (Table II) are dramatically larger than those predicted using the parameters considered in Reference 18. This is evident from a cursory comparison of Figure 1 in Reference 18 to our $(\omega L/10)^{-1} \sim 6R_N^{-1}$ and $(R/10)^{-1} \sim 0.3R_N^{-1}$. The inductance per junction $L/10 \sim 300$ pH is also an order of magnitude higher than the expected adiabatic Josephson inductance $L_J = [2\partial_\Phi I_s(\Phi)]^{-1} \sim 50$ pH, where we approximate the dc supercurrent $I_s(\Phi)$ as $I_c \sin(\pi\Phi/\Phi_0)$ and the critical current I_c as the ideal value $6.7E_T/eR_N$ for $\Delta/E_T = 13$.⁴ Moreover—in the results below—we observe a weak temperature dependence of $R(\Phi = 0)$ measured near 1 GHz, which is in stark contrast to the theoretically predicted exponential dependence.

The observed values of L and R^{-1} imply that the the proximity-induced superconductivity is significantly weaker than expected. We consider two distinct scattering mechanisms as potential explanations for this.

First, we include dephasing due to inelastic scattering by choosing a phenomenological relaxation rate Γ .¹⁸ Second, we include a spin-flip scattering rate Γ_{sf} , which could arise from dilute magnetic impurities in the weak link.³⁰ Specifically, we include the spin-flip scattering as an additional self-energy $\check{\sigma} = -\frac{i}{2}\hbar\Gamma_{\text{sf}}\hat{\tau}_3\check{y}\hat{\tau}_3$ in the equations defined in Reference 18. Although quantitative details differ, both of the scattering mechanisms generally lead to increased dissipation and increased inductance. Increased dissipation occurs mainly due to the suppression of E_{g} , while increased inductance occurs mainly due to the increase in L_{J} .

Theoretical work on the microscopic origin of the scattering rates in disordered metals is reviewed in References 31 and 32. Experiments have also been performed with high-purity metal wires.^{33,34} However, we are not aware of measurements on the gold-palladium alloy used here, which prevents direct comparison to existing literature. Instead, our goal is to estimate the scattering rates required for a qualitative match to the experimental results. We find that in order to reproduce the experimentally observed L or R , the phenomenological rates Γ and Γ_{sf} must be large, i.e., comparable to E_{T}/\hbar and $k_{\text{B}}T/\hbar$.

Inelastic scattering and spin-flip scattering are not the only possible explanations for observing proximity-induced superconductivity that is weaker than what is predicted by the ideal Usadel-equation-based theory. While we do not attempt to exhaustively cover all candidates, we note that the SN contact resistance in our samples is much smaller ($R_{\text{B}} \lesssim 1 \Omega$) than the normal-state resistance ($R_{\text{N}} = 15 \Omega$). While the smallness of the ratio $R_{\text{B}}/R_{\text{N}}$ does not conclusively exclude explanations based on imperfect interfaces, it limits them significantly.^{5,35}

V. TEMPERATURE AND FLUX DEPENDENCE NEAR 1 GHZ

Below, we compare the predicted and observed dependences of Z_{chain} on the bath temperature and magnetic flux. We choose to analyze two low- n resonances near 1 GHz, mainly because the L values we extract for them suffer the least from the uncertainty in f_0 .

Figure 4 shows the measured flux dependence of R and L for the third ($n = 3$) resonance in Sample 2. The bath temperature is $T_{\text{b}} = 195$ mK, which should be high enough for neglecting the hot-electron effect, i.e., for assuming that $T \approx T_{\text{b}}$. As expected, we observe that R and L are periodic in flux, and that the inductance L and the loss tangent $\omega L/R$ are minimized (maximized) at integer (half-integer) values of Φ/Φ_0 .

Figure 4 also includes theoretical predictions for two different rates of inelastic scattering. The weaker of the two rates ($\Gamma = 2.3k_{\text{B}}T_{\text{b}}/\hbar$) reproduces $R(\Phi = 0)$ well and gives a reasonable prediction for its flux-dependent oscillations. Furthermore, if we could only measure changes in L , we might conclude that the predicted flux mod-

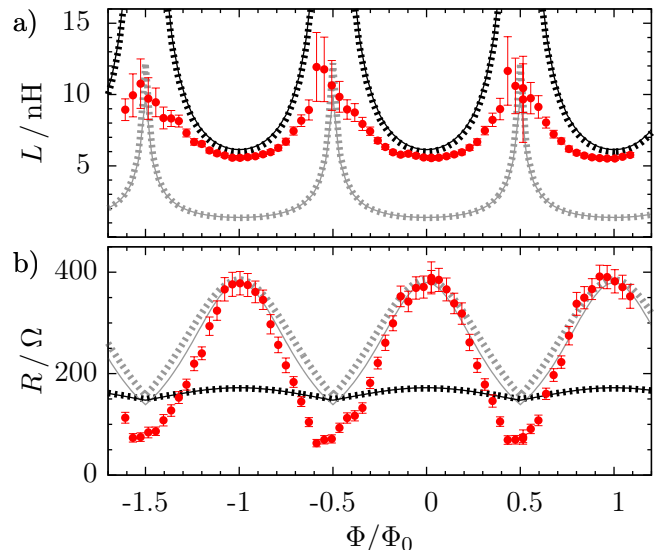


FIG. 4. Flux-dependent a) L and b) R measured near 1.4 GHz of the SQUID chain in Sample 2 at 195 mK. Dashed lines are theoretical calculations that include only inelastic scattering corresponding to a very high scattering rate $\Gamma = 8k_{\text{B}}T_{\text{b}}/\hbar$ (black dashed line) and a moderately high scattering rate $\Gamma = 2.3k_{\text{B}}T_{\text{b}}/\hbar$ (gray dashed line). Solid lines are calculations that include very strong elastic spin-flip scattering, $\Gamma_{\text{sf}} = 15E_{\text{T}}/\hbar$ (black solid line), and moderately strong scattering, $\Gamma_{\text{sf}} = 4.5E_{\text{T}}/\hbar$ (gray solid line). Both solid lines include an additional low inelastic rate of $\Gamma = 0.05k_{\text{B}}T_{\text{b}}/\hbar$.

ulation of L is in fair agreement with the experimental data for this moderate value of Γ . However, the absolute value of the prediction for $L(\Phi)$ is several times smaller than the observed value at nearly all flux values. This highlights the importance of measuring L and R without offsets if theories are to be rigorously tested. Note that we can improve the agreement between the predicted and measured $L(\Phi)$, especially around integer values of Φ/Φ_0 , by using a very strong inelastic scattering rate of $\Gamma = 8k_{\text{B}}T_{\text{b}}/\hbar$ in the theoretical calculation. However, this value of Γ leads to a clear disagreement in the amplitude of the oscillations in $R(\Phi)$ as shown in Figure 4b.

Figure 4 also shows the theoretical predictions that include strong spin-flip scattering. By choosing Γ_{sf} appropriately, the predictions become nearly identical to the case of strong inelastic scattering. Therefore, the conclusions of the previous paragraph also apply to predictions where scattering is spin-flip dominated. Furthermore, the similarity of the predictions shows that, in this parameter regime, the source of additional dephasing is unimportant.

To gain further insight, we study the temperature dependence of $R(\Phi = 0)$ and $L(\Phi = 0)$ for one resonance from each sample near 1 GHz (see Figure 5). In addition to the measured data points, Figure 5 shows theoretical predictions with scattering parameters that—at 195 mK—are identical to those in Figure 4. However, we note

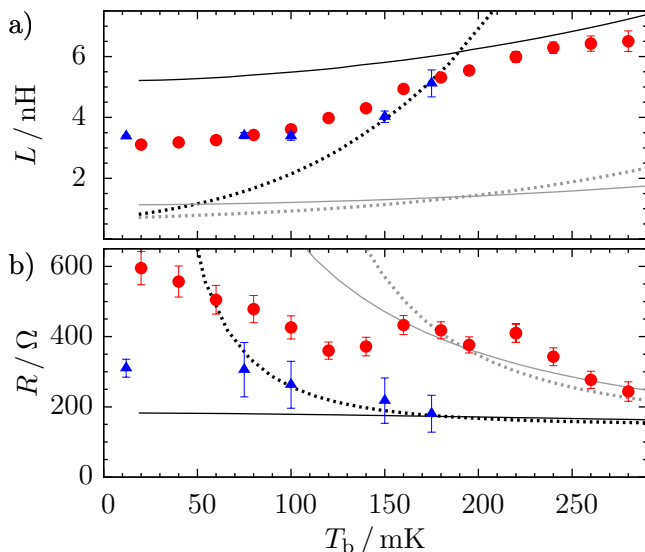


FIG. 5. Temperature dependence of a) $L(\Phi = 0)$ and b) $R(\Phi = 0)$ for Sample 1 near 0.9 GHz (filled triangles) and for Sample 2 near 1.4 GHz (filled circles). The scattering rates for the theoretical predictions are given in Figure 4.

that considerable freedom remains in choosing the temperature dependence of the scattering rates. Rigorously justifying a particular temperature scaling would require knowledge of the specific microscopic mechanism responsible for the scattering. However, as the theoretical predictions already disagree with the measured results at the phenomenological level at a fixed temperature (Figure 4), identifying any specific microscopic mechanism seems implausible. As instructive examples, we choose $\Gamma \propto T$ and a constant Γ_{sf} in Figure 5. Unsurprisingly, none of the predictions simultaneously matches the observed temperature dependence of L and R . Nevertheless, the experimental data in Figure 5 may serve an important role in testing alternative theories in the future.

VI. CONCLUSIONS

The main discrepancy between theory and experiment can be summarized as follows. The proximity effect at $T \lesssim E_T/k_B$ and $\omega \sim E_T/\hbar$ is weaker than what is predicted by theory based on the Usadel equation.¹⁸ This disagreement manifests itself experimentally as measured R values that fall below theoretical predictions and measured L values that exceed theoretical predictions. As potential candidates for such loss of coherence, we considered inelastic scattering and spin-flip scattering in the weak link. However, we did not find choices of Γ or Γ_{sf} that would provide simultaneous agreement in L and R , neither in terms of flux dependence at a fixed bath temperature, nor in terms of temperature-dependence at zero flux bias. Furthermore, the scattering rates required for a match in either L or R are larger than expected for,

e.g., electron–electron scattering in disordered systems.³²

We note that the discrepancies shown here are not in direct contradiction with the previous experiments^{22,23} and that both the SNS junctions and the measurement scheme presented here are very different from these preceding studies. Firstly, the weak link material is different than in the previous experiments. We cannot rule out the possibility of effects specific to gold-palladium³⁶ that reduce coherence in the weak link. Secondly, we measure both the reactive and dissipative components of the electrical admittance without arbitrary offsets. In contrast, only changes in the admittance have been previously reported. Thus, our experimental technique provides a more stringent test of the accuracy of the theory and reveals quantitative disagreements more easily.

In conclusion, we reported measurements of microwave frequency admittance for gold-palladium SNS junctions, together with a comparison to quasiclassical theory for diffusive SNS weak links. These discrepancies between measurement results and theoretical predictions suggest that dephasing caused by inelastic scattering, or elastic spin-flip scattering, is probably not the correct mechanism for explaining why the proximity-induced superconductivity is weaker than expected in our gold-palladium SNS junctions. Further theoretical work is required for reaching simultaneous agreement for the magnitude, temperature dependence, and flux dependence of both the dissipative and reactive parts of the admittance. Mechanisms that may need to be taken into account include imperfect interfaces^{5,35}, electron–electron and fluctuation effects in low-dimensional superconducting structures,^{37,38} and paramagnon interaction.³⁹ Magnetic effects could be particularly important in SNS junctions that include palladium, which is paramagnetic in bulk and can even become ferromagnetic in nanoscale particles.^{40,41} In general, the relationship between microscopic materials properties and coherence at microwave frequency in normal-metal Josephson junctions should be clarified, both experimentally and theoretically. A productive experimental approach may be to first investigate systems such as Nb/Cu weak links that, based on previous dc experiments,^{4,42} are expected to behave in an ideal fashion at dc.

VII. EXPERIMENTAL SECTION

A. Device fabrication

1. Resonators

The substrates are 4" (0.5-mm thick) high-resistivity ($>10^4 \Omega\text{cm}$) Si wafers with 300 nm of thermal oxide. First, a niobium thin film (thickness 200 nm) is sputter deposited on the entire wafer. Next, the coplanar waveguide (CPW) structures are defined with AZ5214E positive photoresist that is reflowed at 150 °C for 1 min to ensure a positive etch profile of the resulting Nb features.

Then CPWs are etched with an rf-generated plasma under a constant flow of SF₆(40 sccm)/O₂(20 sccm) gases at constant power.⁴³ The remaining resist is removed with solvents and an additional O₂-plasma cleaning step. The 4" wafer is then coated with a protective layer of resist and pre-diced with partial cuts along device pixel outlines on the back of the wafer.

2. Capacitor dielectric

The Al₂O₃ dielectric for the on-chip Nb-Al₂O₃-Al capacitors C_C , C_i , and C_{gnd} is formed by atomic layer deposition with 455 cycles in a H₂O/TMA process at 200 °C resulting in a thickness of 42 nm. The thickness was verified in ellipsometry using an index of refraction $n_{\text{Al}_2\text{O}_3} = 1.64$. Measurements of reference Nb-Al₂O₃-Al capacitors yield a capacitance per unit area of 1.4 fF/μm⁻².

3. Nanostructures

The gold-palladium nanowires and aluminum superconducting leads are fabricated by electron beam lithography in two separate evaporation/lift-off steps. In the first step, gold and palladium pellets are evaporated from the same crucible with an electron beam heater. Afterward, unwanted Au-Pd is lifted off with organic solvents. Prior to the evaporation of the Al leads, samples are cleaned in situ with an Ar sputter gun. Finally, after lift-off of the Al film, individual resonator pixels are snapped along the pre-diced lines and packaged for measurement.

The chemical composition of the gold-palladium material is determined with energy-dispersive X-ray spectroscopy for incident electron beam energies 5 keV, 10 keV, and 20 keV (Figure 6). The average Au:Pd atomic ratio (weight ratio) is approximately 3:2 (3:1)

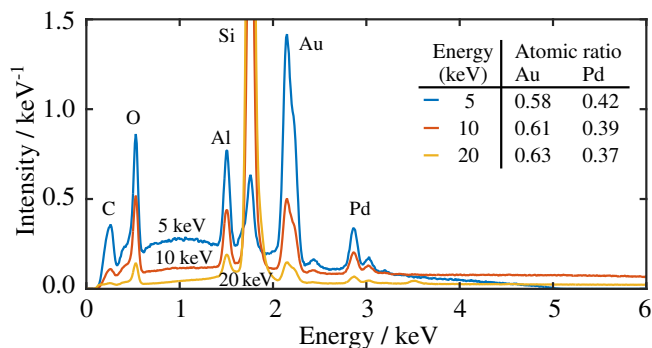


FIG. 6. Measured composition of a section of gold-palladium alloy evaporated together with Sample 2. The material stack from top to bottom is gold-palladium (30 nm), Al₂O₃ (42 nm), SiO₂ (300 nm), and Si (500 μm). For clarity, we crop the strong signal for Si at high electron beam energies. It peaks at 2.8 keV⁻¹ (5.4 keV⁻¹) for 10 keV (20 keV).

B. Cryogenic measurements

Measurements are carried out in a commercial cryostat with the base temperature of 10 mK. The transmission coefficient was probed with a vector network analyzer. The device input line had >100 dB fixed attenuation. For all measurements, the output signal is amplified by a broadband low-noise cryogenic amplifier and by additional room temperature amplifiers. For some measurements (e.g. Sample 2, $n = 3$) two cryogenic isolators are placed on the base cooling stage between the low-noise cryogenic amplifier and the sample. Each sample was placed in a custom printed circuit board and sealed within a metal enclosure. The external flux coil consists of a superconducting solenoid with 100 turns that is fixed outside the metal enclosure. One Φ_0 period in Figure 4 and 5 corresponds to a current change of $\Delta I_{\text{mag}} \approx 7$ mA through the coil. Magnetic shielding surrounds both the enclosure and flux-coil in the case of Sample 2.

The measurement power incident at the transmission line input is approximately -128 dBm for the data shown in Figure 4 and 5. This drives a current of roughly 5 nA through the SQUID chain at $\Phi = 0$ for $n = 3$ of Sample 2. This is far below the estimated critical current of the SQUID chain. Furthermore, experimentally we ensure that we measure the linear response by making sure that the measured S_{21} is not sensitive to factor-of-two changes in the measurement power.

C. Normalized transmission coefficient

We define the normalized transmission coefficient S_{21} as $S'_{21}(\Phi)/[S'_{21}(\Phi_{\text{ref}})/S_{21,\text{fit}}(\Phi_{\text{ref}})]$, where $S'_{21}(\Phi)$ is the full transmission coefficient, including contributions from the cabling and other external circuitry, and $S_{21,\text{fit}}$ is its best fit to Equation 1. Dividing by $S'_{21}(\Phi_{\text{ref}})$ removes all flux-independent features introduced external circuitry and unintentional reflections. Multiplying by $S_{21,\text{fit}}$ removes the systematic contribution of the reference, which would otherwise appear at all values of Φ as a static vertically inverted mirror image ($|S_{21,\text{fit}}| > 1$) of the reference resonance.

The scan used as the reference alternates between $\Phi_{\text{ref}} = \Phi_0/2$ and $\Phi_{\text{ref}} = 0$, changing from one to the other whenever Φ crosses $\Phi_0(1/4 + k/2)$, where $k \in \mathbb{Z}$. This keeps the resonance in the reference far from the resonance frequency at the Φ value being analyzed. These changes in Φ_{ref} cause the apparent discontinuities in the background color in Figure 2.

ACKNOWLEDGEMENTS

We thank Leif Grönberg for depositing the Nb used in this work. We acknowledge the provision of facilities and technical support by Aalto University at OtaNano - Micronova Nanofabrication Centre as well as financial

support from the Emil Aaltonen Foundation, the European Research Council under Grant 278117 (SINGLE-OUT), the Academy of Finland under The COMP Centre of Excellence (251748, 284621) and grants 257088, 265675, 276528, 286215 and the European Metrology Re-

search Programme (EMRP EXL03 MICROPHOTON). The EMRP is jointly funded by the EMRP participating countries within EURAMET and the European Union. We also acknowledge support from Aalto Centre for Quantum Engineering.

-
- ¹ J. Clarke, *Phys. Rev. Lett.* **21**, 1566 (1968).
² K. D. Usadel, *Phys. Rev. Lett.* **25**, 507 (1970).
³ K. K. Likharev, *Rev. Mod. Phys.* **51**, 101 (1979).
⁴ P. Dubos, H. Courtois, B. Pannetier, F. K. Wilhelm, A. D. Zaikin, and G. Schön, *Phys. Rev. B* **63**, 064502 (2001).
⁵ T. T. Heikkilä, J. Särkkä, and F. K. Wilhelm, *Phys. Rev. B* **66**, 184513 (2002).
⁶ H. Courtois, M. Meschke, J. T. Peltonen, and J. P. Pekola, *Phys. Rev. Lett.* **101**, 067002 (2008).
⁷ A. F. Andreev, *Sov. J. Exp. Theor. Phys.* **22**, 455 (1965).
⁸ S. Guéron, H. Pothier, N. O. Birge, D. Esteve, and M. H. Devoret, *Phys. Rev. Lett.* **77**, 3025 (1996).
⁹ H. le Sueur, P. Joyez, H. Pothier, C. Urbina, and D. Esteve, *Phys. Rev. Lett.* **100**, 197002 (2008).
¹⁰ H. A. Notarys, M. L. Yu, and J. E. Mercereau, *Phys. Rev. Lett.* **30**, 743 (1973).
¹¹ J. M. Warlaumont, J. C. Brown, T. Foxe, and R. A. Buhrman, *Phys. Rev. Lett.* **43**, 169 (1979).
¹² K. W. Lehnert, N. Argaman, H. R. Blank, K. C. Wong, S. J. Allen, E. L. Hu, and H. Kroemer, *Phys. Rev. Lett.* **82**, 1265 (1999).
¹³ P. Dubos, H. Courtois, O. Buisson, and B. Pannetier, *Phys. Rev. Lett.* **87**, 206801 (2001).
¹⁴ M. Fuechsle, J. Bentner, D. A. Ryndyk, M. Reinwald, W. Wegscheider, and C. Strunk, *Phys. Rev. Lett.* **102**, 127001 (2009).
¹⁵ F. Chiodi, M. Aprili, and B. Reulet, *Phys. Rev. Lett.* **103**, 177002 (2009).
¹⁶ P. Virtanen, T. T. Heikkilä, F. S. Bergeret, and J. C. Cuevas, *Phys. Rev. Lett.* **104**, 247003 (2010).
¹⁷ A. V. Galaktionov and A. D. Zaikin, *Phys. Rev. B* **82**, 184520 (2010).
¹⁸ P. Virtanen, F. S. Bergeret, J. C. Cuevas, and T. T. Heikkilä, *Phys. Rev. B* **83**, 144514 (2011).
¹⁹ F. Kos, S. E. Nigg, and L. I. Glazman, *Phys. Rev. B* **87**, 174521 (2013).
²⁰ M. Ferrier, B. Dassonneville, S. Guéron, and H. Bouchiat, *Phys. Rev. B* **88**, 174505 (2013).
²¹ K. S. Tikhonov and M. V. Feigel'man, *Phys. Rev. B* **91**, 054519 (2015).
²² F. Chiodi, M. Ferrier, K. Tikhonov, P. Virtanen, T. T. Heikkilä, M. Feigelman, S. Guéron, and H. Bouchiat, *Sci. Rep.* **1**, 3 (2011).
²³ B. Dassonneville, M. Ferrier, S. Guéron, and H. Bouchiat, *Phys. Rev. Lett.* **110**, 217001 (2013).
²⁴ J. Govenius, R. E. Lake, K. Y. Tan, V. Pietilä, J. K. Julin, I. J. Maasilta, P. Virtanen, and M. Möttönen, *Phys. Rev. B* **90**, 064505 (2014).
²⁵ J. Govenius, R. E. Lake, K. Y. Tan, and M. Möttönen, *Phys. Rev. Lett.* **117**, 030802 (2016).
²⁶ J. M. Pomeroy and H. Grube, *J. Appl. Phys.* **105**, 094503 (2009).
²⁷ F. C. Wellstood, C. Urbina, and J. Clarke, *Phys. Rev. B* **49**, 5942 (1994).
²⁸ K. Geerlings, S. Shankar, E. Edwards, L. Frunzio, R. J. Schoelkopf, and M. H. Devoret, *Appl. Phys. Lett.* **100**, 192601 (2012).
²⁹ M. S. Khalil, M. J. A. Stoutimore, F. C. Wellstood, and K. D. Osborn, *J. Appl. Phys.* **111**, 054510 (2012).
³⁰ A. A. Abrikosov and L. P. Gor'kov, *Zh. Eksp. Teor. Fiz.* **39**, 1781 (1960), [*Sov. Phys. JETP*, **12**, 1243 (1961)].
³¹ F. Giazotto, T. T. Heikkilä, A. Luukanen, A. M. Savin, and J. P. Pekola, *Rev. Mod. Phys.* **78**, 217 (2006).
³² J. Rammer and H. Smith, *Rev. Mod. Phys.* **58**, 323 (1986).
³³ F. Pierre, A. B. Gougam, A. Anthore, H. Pothier, D. Esteve, and N. O. Birge, *Phys. Rev. B* **68**, 085413 (2003).
³⁴ B. Huard, A. Anthore, F. Pierre, H. Pothier, N. O. Birge, and D. Esteve, *Solid State Commun.* **131**, 599 (2004).
³⁵ J. C. Hammer, J. C. Cuevas, F. S. Bergeret, and W. Belzig, *Phys. Rev. B* **76**, 064514 (2007).
³⁶ W. C. McGinnis and P. M. Chaikin, *Phys. Rev. B* **32**, 6319 (1985).
³⁷ B. N. Narozhny, I. L. Aleiner, and B. L. Altshuler, *Phys. Rev. B* **60**, 7213 (1999).
³⁸ A. G. Semenov, A. D. Zaikin, and L. S. Kuzmin, *Phys. Rev. B* **86**, 144529 (2012).
³⁹ T. Kontos, M. Aprili, J. Lesueur, X. Grison, and L. Dumoulin, *Phys. Rev. Lett.* **93**, 137001 (2004).
⁴⁰ T. Shinohara, T. Sato, and T. Taniyama, *Phys. Rev. Lett.* **91**, 197201 (2003).
⁴¹ B. Sampedro, P. Crespo, A. Hernando, R. Litrán, J. C. S. López, C. L. Cartes, A. Fernandez, J. Ramírez, J. G. Calbet, and M. Vallet, *Phys. Rev. Lett.* **91**, 237203 (2003).
⁴² R. N. Jafdaraghi, J. T. Peltonen, O.-P. Saira, and J. P. Pekola, *Appl. Phys. Lett.* **108**, 042604 (2016).
⁴³ B. J. Curtis and H. Mantle, *J. Vac. Sci. Technol. A* **11**, 2846 (1993).